

TWENTYFIFTH EUROPEAN ROTORCRAFT FORUM

Paper N° P1

**AIRLOADS MEASUREMENTS FROM A 1/4-SCALE
TILTROTOR WIND TUNNEL TEST**

BY

Stephen M. Swanson
Senior Research Engineer
Aerospace Computing Inc.
Moffett Field, CA USA

Megan S. McCluer
Aerospace Engineer
NASA Ames Research Center
Moffett Field, CA USA

Gloria K. Yamauchi
Aerospace Engineer
NASA Ames Research Center
Moffett Field, CA USA

Alexandra A. Swanson
Senior Research Engineer
Aerospace Computing Inc.
Moffett Field, CA USA

SEPTEMBER 14-16, 1999
ROME
ITALY

ASSOCIAZIONE INDUSTRIE PER L'AEROSPAZIO; I SISTEMI E LA DIFESA
ASSOCIAZIONE ITALIANA DE AERONAUTICA ED ASTRONAUTICA



1. Abstract

Blade airloads data were acquired for a 1/4-scale tiltrotor model tested at the Duits-Nederlandse Windtunnel in The Netherlands. For the first time, detailed airloads measurements were acquired for an isolated tiltrotor model utilizing one hundred and fifty dynamic pressure transducers. Simultaneous acoustic measurements were made in a plane below the model rotor to correlate airloads with tiltrotor noise. Rotor performance data and wake geometry data were also acquired. Samples of the airloads data are presented for several key operating conditions. The effects of rotor thrust and model shaft angle on the blade airloads are discussed. Comparisons are made between blade pressure data, acoustic data and laser light sheet results. Negative lift at the blade tip was found over a wide range of conditions for the tiltrotor in helicopter mode. Single and multiple blade-vortex interactions were measured and correlated with acoustic data and measured wake geometry. The data acquired during this test provide a fundamental set of aeroacoustic measurements that can be used to validate tiltrotor analyses.

2. Nomenclature

A	Rotor area, πR^2 , ft ²
a_∞	Free stream speed of sound, ft/sec
BVI	Blade vortex interaction
c_p	Coefficient of pressure, $(P - P_\infty) / 1/2\rho u_T^2$
c_N	Local blade normal force coefficient, $(\int P_L - \int P_U) / (q_r c_r)$
c_r	Local blade chord, ft
C_T	Rotor thrust coefficient, Thrust/ $\rho A(\Omega R)^2$
LLS	Laser light sheet
M_{tip}	Hover tip Mach number, $\Omega R / a_\infty$
P	Local pressure relative to P_∞ , psi
P_∞	Tunnel static pressure, psia
q_r	Local dynamic pressure, $1/2\rho u_T^2$, psf
R	Rotor radius, ft
r	Local blade radius, ft
RAS	Rotating Amplifier System
TRAM	Tilt Rotor Aeroacoustic Model
u_T	Local velocity, $\Omega r + V \sin \psi$, ft/sec

V	Wind tunnel test section velocity, ft/sec
α_s	Rotor shaft angle, deg, shaft vertical at zero degrees, positive aft
ρ	Free stream air density, slugs/ft ³
μ	Advance ratio, $V / \Omega R$
ψ	Rotor azimuth, deg
Ω	Rotor rotational speed, rad/sec

3. Introduction

Airport congestion is becoming one of the biggest problems facing the air transport industry today. A large percentage of the flights that are conducted in and out of conventional airports are relatively short distance flights with a small number of passengers. The tiltrotor is seen as a viable alternative for reducing airport congestion by relieving the number of flights that require runway access. NASA has invested heavily in tiltrotor research over the past decade to address many of the technical challenges facing tiltrotors. One of the primary goals of the NASA Short Haul (Civil Tiltrotor) (SH(CT)) project (Ref. 1) has been to identify and reduce the noise generation mechanisms of tiltrotors to ensure the successful introduction of these versatile aircraft to the public. The Tilt Rotor Aeroacoustic Model (TRAM) experimental program was developed within the SH(CT) project to help achieve these goals. The TRAM program consists of a series of aeroacoustic wind tunnel tests designed to acquire data necessary for validating aerodynamic, acoustic and performance prediction analyses, such as the NASA Tiltrotor Aeroacoustic Code (TRAC) described in Ref. 2. References 3 and 4 provide detailed descriptions of the isolated and full-span configurations of the TRAM and its capabilities.

The first aeroacoustic test of the isolated rotor configuration of the TRAM was conducted during April-May 1998 in the Duits-Nederlandse Windtunnel Large Low-speed Facility (DNW-LLF). Figure 1 shows the isolated rotor installed in the open-jet test section of the DNW anechoic facility. On the right side of the figure can be seen the acoustic traverse, used to acquire acoustic data in a plane below the rotor. Performance, acoustics, blade airloads, and flow measurement data were acquired during this test. Reference 5 presents an overview of the TRAM DNW test, while Refs. 6 and 7 address the acoustic and flow measurement results, respectively.

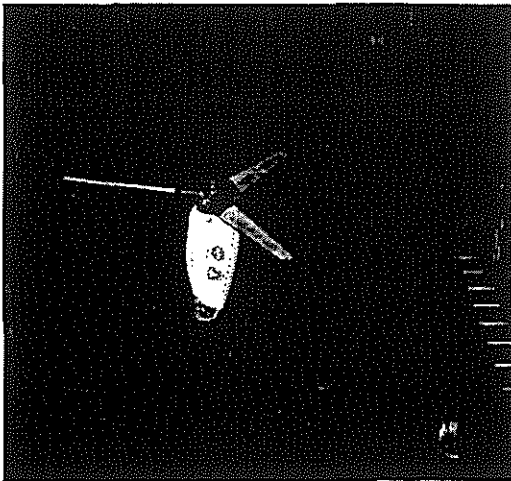


Figure 1. The TRAM rotor installed in the DNW-LLF test section

The data acquired during this test were the first blade airloads data of a tiltrotor in forward flight. Previous investigations presented results for conventional helicopter rotors, ranging from small-scale wind tunnel tests (Refs. 8-11) to full-scale flight data (Refs. 12 and 13). Airloads data on a small-scale tiltrotor in hover were documented in Ref. 14 and wake geometry measurements in hover were made using the shadowgraph technique (Ref. 15).

The aerodynamics of a tiltrotor blade is different from a conventional helicopter blade. Tiltrotor blades have a higher built-in twist, higher blade tip speeds, and higher blade loading than conventional helicopter blades. Existing analytical and empirical models developed for helicopter rotors have not been validated for tiltrotors. This is especially true for the wake geometry model of a tiltrotor. In descent conditions during which blade-vortex interactions (BVI) can occur, tiltrotor blades can undergo negative tip loading over a substantial region of the rotor disk compared with conventional helicopter blades. The negative tip loading causes dual vortices, of opposite sign, to be shed from a single blade. The dual vortices greatly complicate the wake geometry and present a challenge to the analyst trying to model the wake. Less is understood about the aeroacoustics of tiltrotors than helicopters because of these differences in rotor aerodynamics and lack of experimental data.

The data acquired during the TRAM DNW test provides experimental results to help improve the understanding of tiltrotor aerodynamics, wake structure and associated noise sources. Current studies utilizing the

TRAC code (Ref. 16) are comparing TRAM data with analytical acoustic predictions.

This paper provides a general description of the isolated TRAM and detailed descriptions of the blade pressure instrumentation and acquisition. Blade loading trends with changing test conditions are presented and discussed. Comparisons between blade pressure data, acoustic data and laser light sheet results are also presented.

4. Model and Facility Description

The isolated TRAM rotor was tested in the open jet test section of the Duits-Nederlandse Windtunnel Large Low-speed Facility (DNW-LLF) in The Netherlands. The atmospheric open-jet configuration is 8 x 6 meters and is surrounded by a large (23,000 m³) anechoic testing hall (Ref. 17). The test section and hall offer excellent flow quality with low background noise up to 85 knots (Ref. 18) with a maximum speed of 120 knots. The model support sting mechanism has three degrees of freedom and the facility supports an in-flow traversing microphone system.

The isolated TRAM rotor is a three-bladed, 9.5-foot (2.89 m) diameter tiltrotor and is 0.25-scale of the right-hand V-22 Osprey tiltrotor. The blades were designed and fabricated to be statically and dynamically similar to the full-scale V-22 blades. The gimbaled rotor hub is similar to the V-22 hub and is mounted on a six-component force and moment balance. A rotating amplifier system is used to amplify the pressure transducer output voltage in the rotating frame which improves the signal-to-noise ratio of the pressure transducers. A 300-channel slip ring was used to transmit measurements to the non-rotating frame. A more detailed discussion on the TRAM model can be found in Ref. 3.

Shaft angle changes ranged from horizontal for airplane mode to just aft of vertical for helicopter mode. Small shaft angle changes were made using the DNW model support sting while larger changes (between airplane and helicopter modes) were conducted mechanically between test runs. For operational reasons, the testing in helicopter mode was conducted at a rotor speed of 1,415 RPM (tip speed = 214 m/sec, $M_{tip} = 0.63$), 88% of the V-22 hover tip speed. For airplane mode testing, 100% V-22 rotor speed was achievable for a nominal $M_{tip} = 0.59$.

One blade was strain-gauged for safety of flight monitoring and acquisition of blade

structural loads. These included flapwise and chordwise bending moment gauges and blade torsion moment gauges.

5. Airloads Measurements

One hundred and fifty dynamic pressure transducers, distributed across the upper and lower surfaces of two blades, were used to acquire airloads data. Seventy-four and seventy-six transducers populated 8 radial stations of Blade 1 and Blade 2, respectively. The layout of the pressure transducers is shown in Fig. 2. Additional spanwise pressure transducers were installed at $x/c = 3.5\%$ for a range of radial stations.

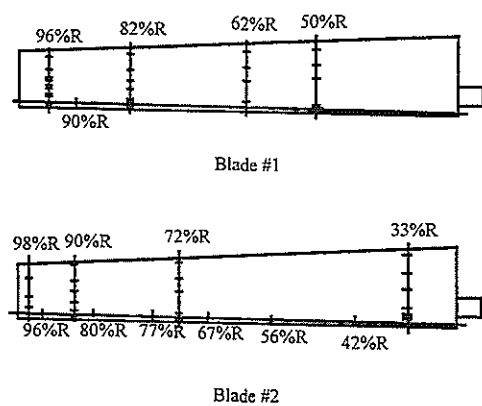


Figure 2. Pressure transducer distribution for blades #1 and #2.

Three types of transducers were installed: pipettes, B-screen, and flat-pack, two of which are shown in Fig. 3. All types used the same measurement device but with different installation. The pipettes were located in the blade leading edge beneath the blade surface. They were connected to the blade surface via a small pipe. The B-screen transducers were located mid-chord, mounted just below the blade surface. These had a small, multi-holed cover plate between the transducer and the blade surface. The flat-pack transducers were flush mounted on the blade, with the transducer located at the surface. The transducers had a measurement range of 0 to 25 psia and, according to manufacturer specifications, had a flat frequency response out to 60 kHz (within 0.5 dB). The pipette type installation, which was at the blade leading edge, was expected to have a reduced bandwidth due to a short pipe connecting the transducer to the blade surface.

A dynamic frequency check was conducted prior to the test to determine the

installed dynamic characteristics. Methods similar to those discussed in Ref. 19 were used to acquire and process the dynamic results. The majority of pressure transducers demonstrated a flat frequency response out to 10 kHz (425/rev, the maximum accurate frequency of the calibration hardware) and it was determined that the pipette transducers were not adversely affected by installation. The criteria for acceptance was a flat phase and amplitude response (to within 1%) out to 10 kHz when cross-correlated with a reference transducer. Any transducer that did not meet this specification was either replaced or flagged as non-functional throughout the test program. At the start of the test, 19 transducers were non-functional.

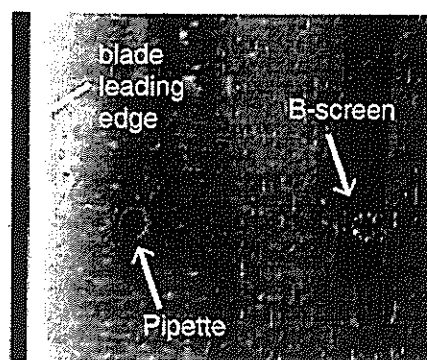


Figure 3. Photograph of a pipette and B-screen pressure transducers installation on the blade upper surface.

The pressure data were acquired at 2048 samples per revolution over 64 revolutions and were acquired simultaneously with rotor performance and acoustic data. The transducer output signals were transmitted through a braided wire bundle within the rotor shaft. The signals were amplified in the rotating frame by the Rotating Amplifier System (RAS) before being fed through a slip ring. The RAS was an on-board amplifier and signal conditioner system built specifically for the TRAM by the National Lucht-en Ruimtevaartlaboratorium (NLR). Reference 20 discusses the capabilities of the RAS in more detail. From the slipring, the output signals were passed to the control room and conditioned by low-pass filters set at 20 kHz. The 20 kHz filter setting was chosen to evaluate broadband blade pressure and acoustic data. No attempt has yet been made to calibrate and correlate the blade pressure data above 10 kHz to accurately evaluate broadband data.

Data were digitized using a 16-bit machine and stored in binary files. Data reduction was primarily conducted on a post-test basis due to the large amount of data acquired for each point. A few select channels were viewed on a real-time basis using oscilloscopes to help in test operations. The raw data were evaluated between runs to adjust the RAS gain settings as a means to optimize the transducer signal-to-noise ratio.

In addition to the pre-test dynamic frequency checkout, the pressure transducers were statically calibrated both before and during the test. Before the test, the blades were installed in a rigid, sealed calibration tube where the pressure was cycled from 0 to 25 psia. During the test, with the blades installed on the model, a vacuum bag system was utilized to conduct daily, suction pressure calibrations. All functional transducers had a linear conversion from output volts to engineering units.

A standard repeat point was acquired at the start of each run with the rotor and tunnel set to a specific condition. Figure 4 is an overlay of averaged time histories of 5 standard repeat points from different days during the test. The repeatability of the acquired signal during the test program is shown to be within 1/2% of full-scale.

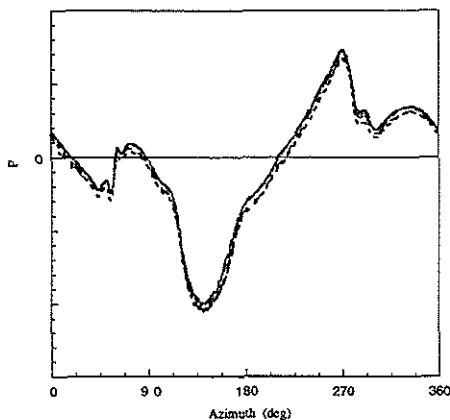


Figure 4. Repeat standard condition data points, $r/R = 93\%$, $x/c = 3.5\%$, lower surface.

Data acquired over the 64 rotor revolutions for each data point was also found to be very repeatable. Figure 5 shows data for one channel for all 64 rotor revolutions. The stability of the transducers over the approximately 2.5 seconds of data acquisition is

shown here and is typical of data throughout the test program.

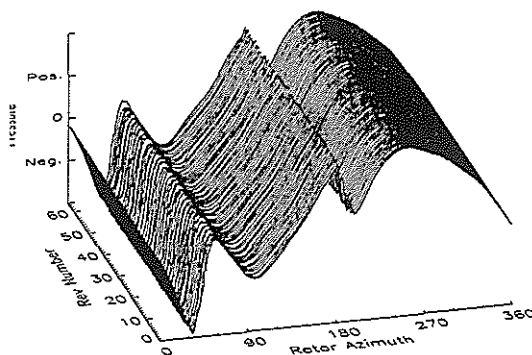


Figure 5. Repeatability over 64-revolutions.

6. Data Reduction

The blade airloads were processed using a NASA in-house program, written to both evaluate the quality of the data and to process the data into pressure coefficient (C_p) and/or normal force coefficient (C_N). An automated computer program was used to review each of the 2048 samples per rev for data quality. The program checked whether any samples saturated the limits of the data acquisition hardware. If one or more samples in a rotor revolution were saturated, that revolution was flagged as unusable. In addition to the automated process, each channel was manually reviewed for anomalies such as excessive electronic noise, sharp spikes or signal loss. Any recorded rotor revolution with bad data samples was flagged as unusable.

The pressure data were then converted from computer counts to engineering units. This step also corrected the data for the specific amplifier gain applied by the RAS. Equation 1 highlights this first step.

$$EU = (\text{data} / \text{gain}) * \text{slope} \quad (1)$$

The RAS has the capability to adjust the voltage output of the pressure transducers to approximately 0 volts at ambient pressure, however it was not always possible to achieve exactly 0 volts. A non-rotating data point was acquired at the start of each run to account for any remaining offset. This data point was subtracted from the pressure transducer output during data reduction to complete the balance process. The data was then corrected by adding the tunnel static pressure, P_∞ for the non-

rotating data point. Measured pressure relative to P_∞ was calculated for each point by subtracting P_∞ for that point (Equation 2).

$$P = \{ (EU - EU_{\text{non-rotating}}) + P_{\infty, \text{non-rotating}} \} - P_\infty \quad (2)$$

One averaged revolution of data was calculated from the 64 revs acquired for each transducer. The pressure measurements were then plotted as a function of azimuth (ψ) for individual transducers or for a set of transducers (chordwise, spanwise, upper and lower). The c_p for each transducer was then calculated as a function of the local velocity (Equation 3) or local Mach number (Equation 4). For data presented in this paper, the c_p is nondimensionalized by the local velocity.

$$c_p = \frac{P}{\frac{1}{2}\rho(\Omega r + V_\infty \sin \psi)^2} \quad (3)$$

$$M^2 c_p = \frac{P}{\frac{1}{2}\rho(a_\infty)^2} \quad (4)$$

To calculate the blade normal force per unit span, the difference between the integrated upper and lower surface pressures was computed and then normalized by the local dynamic pressure ($q_r = 1/2\rho u_T^2$) and local blade chord (c_r) (Equation 5).

$$c_N = \frac{\int_0^c P_L dx - \int_0^c P_U dx}{q_r c_r} \quad (5)$$

The integration routine used to calculate c_N was a 5-point Newton-Cotes integration formula, which required a minimum of four functional pressure transducers for each upper and lower surface chordwise station. It was not always possible to generate c_N values for some test conditions, especially for data acquired towards the end of the test program, when many of the blade pressure signals were not acquired due to fatigue problems with wiring harnesses.

For the TRAM, as with most small-scale rotor models, measuring pressure at the blade leading and trailing edges was physically not possible. It was required to estimate the pressures at the leading edge and the trailing edge in order to complete integration for c_N . Either the leading edge and trailing edge pressures were assumed to be 0.0 or were calculated as a mean between the closest functional upper and lower surface transducers. Figure 6 presents data for the two different methods with the leading and trailing edge values set to 0.0 and to the calculated means. Only slight differences in the c_N values are discernable. For the data presented in this paper, means between the upper and lower transducers closest to the leading and trailing edges were calculated prior to completing the integration.

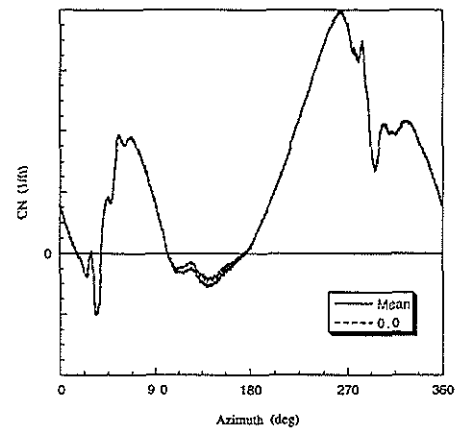


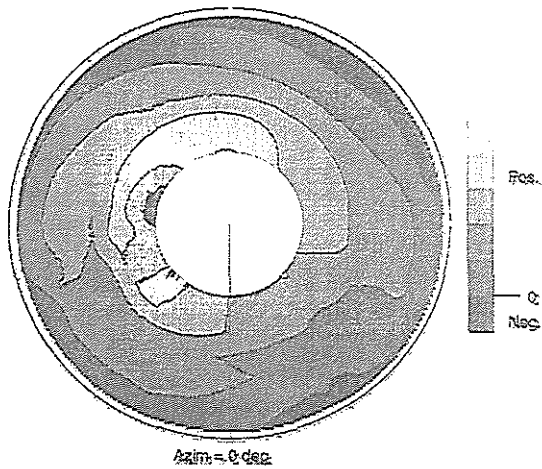
Figure 6. Effect of different c_N calculations on resultant time traces.

7. Results

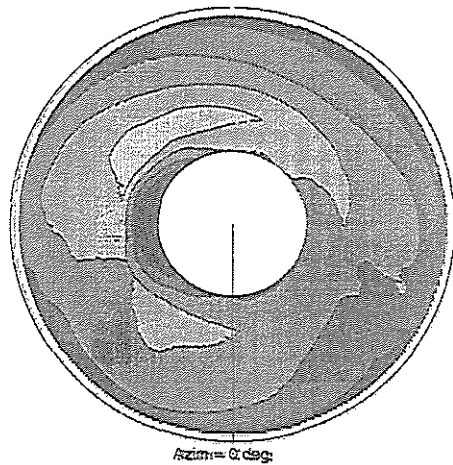
Data are presented for changes in the blade airloads with variations in rotor shaft angle (α_s) and rotor thrust coefficient (C_T). Comparisons between airloads data, acoustic data and laser light sheet results are discussed. The blade airloads are displayed using contour plots of the c_N values. For all contour plots, the wind tunnel flow is from the top of the page and the lighter color indicates higher positive c_N values. The rotor rotation is counter-clockwise as seen from above. c_p values for individual pressure taps are presented when more specific details are desired.

Variation in shaft angle. A comparison of data for a variation of shaft angles with $\mu=0.15$ and low C_T is shown in Fig. 7 (α_s is negative with

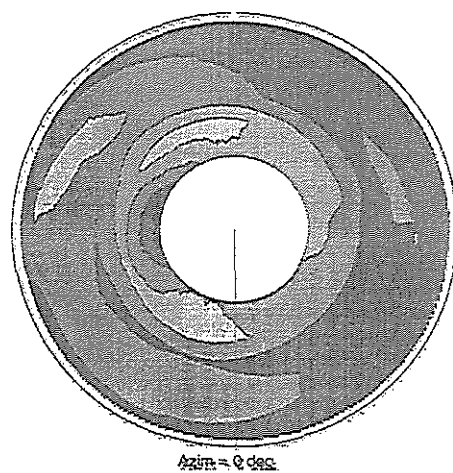
the shaft tilted forward). These circular contour plots display the c_N values for the rotor disk, with rotor rotation counter-clockwise. For the positive shaft angle condition (Fig. 7a), the blade tip ($r/R > 90\%$) is negatively loaded for a



a) c_N contour for positive α_s



b) c_N contour for zero α_s



c) c_N contour for negative α_s

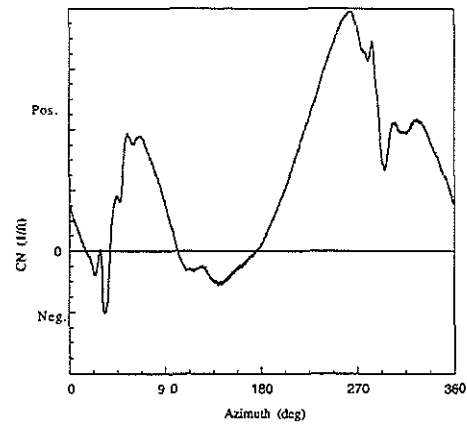
Figure 7. Variation of α_s , $\mu = 0.15$, low C_T .

range of ψ from approximately 20 deg to 50 deg and again from 100 deg to 190 deg. The

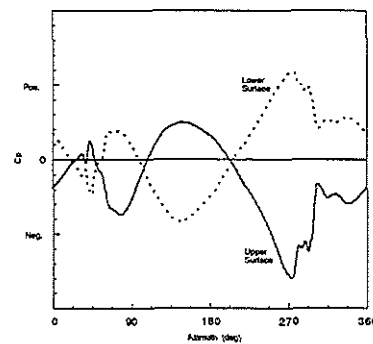
region of negative tip loading decreases as α_s is reduced to a negative angle. Figure 7b also shows a region of negative c_N values occurring at the blade root for $250 \text{ deg} < \psi < 280 \text{ deg}$. Figure 8a shows a time trace of the c_N values for $r/R = 90\%$ for the positive α_s condition and

Fig. 8b shows the associated c_p values for transducers near the leading edge. For $100 \text{ deg} < \psi < 190 \text{ deg}$, the upper surface transducer measured a positive pressure while the lower surface measured a negative pressure. This is a result of the high blade twist required by the tiltrotor for operation in airplane mode and is most noticeable at the positive α_s and low thrust loading conditions.

A sharp peak in both the upper and lower c_p measurements occurs at $\psi = 40 \text{ deg}$, typical of a blade-vortex interaction (Fig. 8b).



a) c_N values.

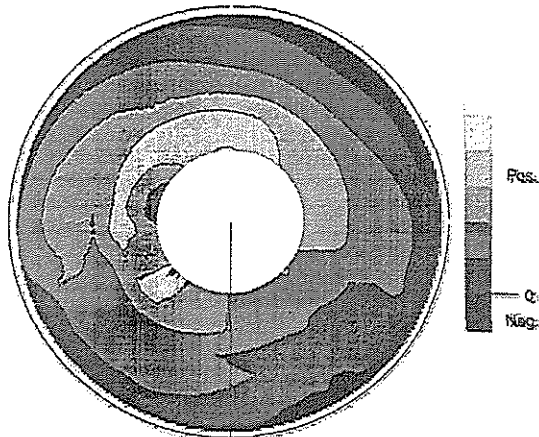


b) c_p time trace $x/c=6.5\%$.

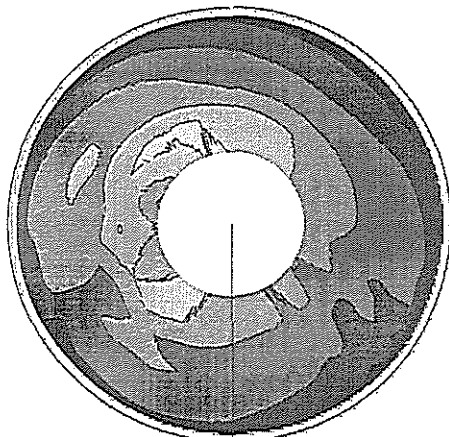
Figure 8. c_N and c_p data for: $r/R = 90\%$, positive α_s , $\mu = 0.15$, low C_T .

Variation in rotor thrust. Comparisons of c_N for

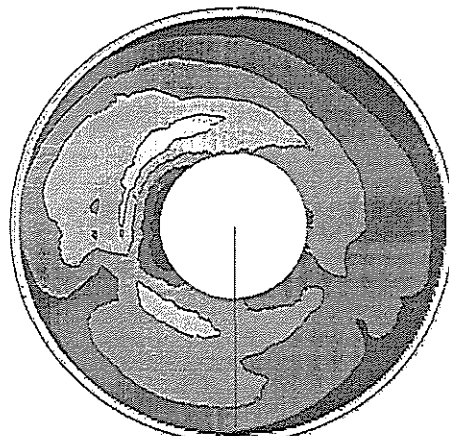
positive α_s and $\mu = 0.15$ but with increasing C_T are shown in Fig. 9. As C_T increases, c_N increases and the azimuth range with negative tip loading decreases. The reduction in the negative tip loading is a result of the increased blade angle and resultant inflow angle. Figures 9b and 9c also show an increase in the



a) c_N contour for low C_T .



b) c_N contour for medium C_T .

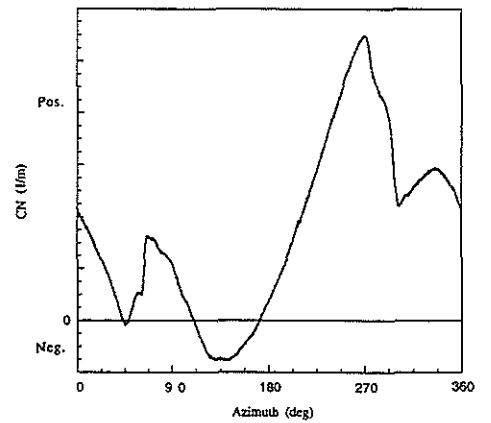


c) c_N contour for high C_T .

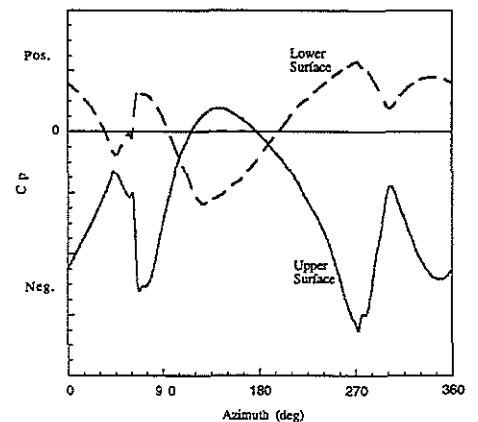
Figure 9. Variation of c_N for positive α_s , $\mu = 0.15$.

unsteadiness of the c_N measurements near $\psi = 45$ deg. This unsteadiness is a result of multiple wake interactions. Figure 10 presents c_N values for $r/R = 90\%$ and corresponding c_p values for upper and lower leading edge pressure transducers at $x/c = 3.5\%$ for the condition corresponding to Fig. 9c. Figure 10a shows that the negative c_N has been reduced to a small ψ range near 45 deg and 135 deg.

Comparison with Acoustic Data. One of the objectives of this test was to acquire simultaneous blade pressure measurements and acoustic data. Data were successfully acquired for a wide range of conditions, primarily associated with simulated descent conditions when BVI noise dominate. Multiple BVI were



a) c_N time history



b) Upper and Lower c_p time histories for $x/c = 3.5\%$

Figure 10. Blade c_N and c_p values for: $r/R = 96\%$, positive α_s , $\mu=0.15$, high C_T .

measured with the microphones below the plane of the rotor for the high thrust condition. Figure 11 shows an acoustic time trace for one of the microphones ($x = -0.69$ m, $y = 0.93$ m) with several interactions occurring on the blade. Blade vortex interactions are classified by how the blade and vortex interact, either parallel, oblique or perpendicular. The airloads measurements were useful in determining the type of vortex interaction occurring. Figure 12 shows a series of pressure measurements all at the same chordwise location but at different spanwise locations (each time trace is vertically offset for clarity). The multiple vortex interactions occur along the entire measured span of the blade, indicating that these are parallel or nearly parallel interactions.

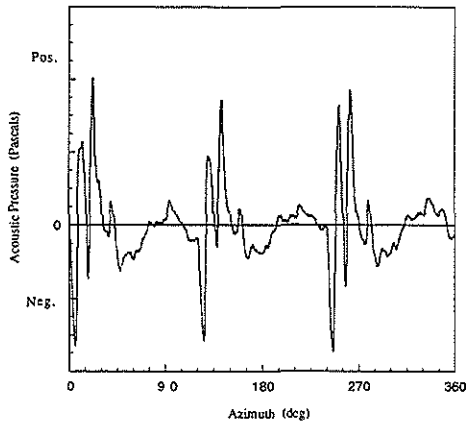


Figure 11. Acoustic measurements for: $x_{mic} = -0.69$ m, $y_{mic} = 0.93$ m, positive α_s , $\mu = 0.15$, high C_T .

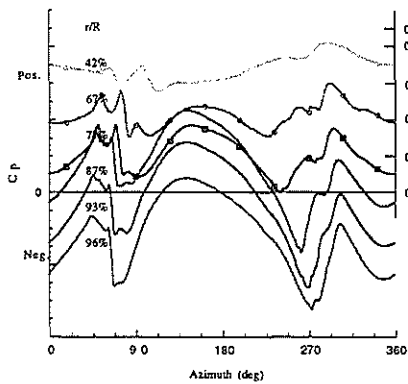
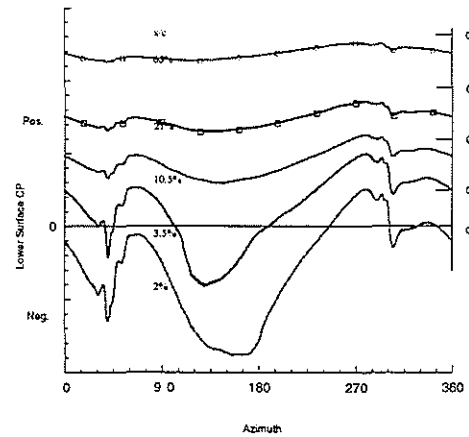
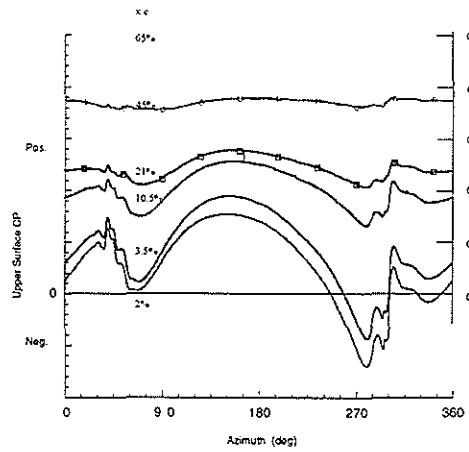
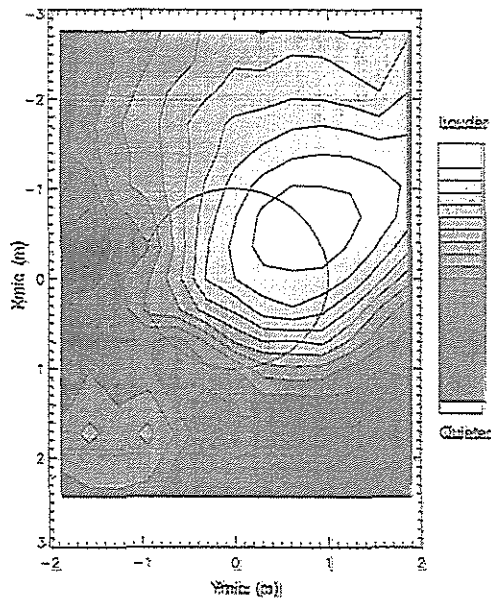


Figure 12. Upper surface spanwise c_p values for: $x/c = 3.5\%$, positive α_s , $\mu = 0.15$, high C_T .

A comparison between blade airloads and acoustics is shown in Fig. 13.



a) Upper and lower surface c_p traces for: $r/R = 96\%$, $\mu = 0.15$, positive α_s and low C_T .



b) Acoustic traverse contour
Figure 13. Blade pressure and acoustic data for: $\mu = 0.15$, positive α_s and low C_T .

Figure 13a presents upper and lower surface c_p values for $r/R = 96\%$ station and shows a very strong pressure pulse at $\psi = 45$ deg (note that the c_p plots are vertically offset for clarity). Figure 13b presents acoustic data for a sweep of the traverse below the plane of the rotor for the same test condition. Data in this plot are sound pressure level calculations for a range between the 7th and 50th blade passage frequencies, which contain a majority of the acoustic energy of a BVI. The wind is from the top of the page down and the circle in the center of the figure represents the rotor. This acoustic contour also corresponds with the blade pressure contour shown in Fig. 7a. Figure 13b shows an area of strong acoustic energy on the advancing side of the rotor. Figure 14 shows a time trace of the acoustic data acquired at this high-energy location. A strong acoustic pulse was measured for each blade passage. The acoustic pulse is associated with the pressure pulse measured with the transducers (Fig. 13a).

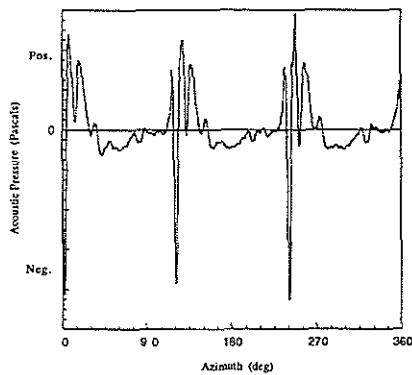


Figure 14. Acoustic time history for: $x_{mic} = -0.69$ m, $y_{mic} = +0.93$ m, $\mu = 0.15$, positive α_x , and low C_T .

Comparison with Laser Light Sheet. Several runs were conducted during the test in which the laser light sheet (LLS) technique was used to collect wake geometry data on the rotor advancing side. The wake geometry data were useful in defining the location of blade vortices with respect to the blade. Reference 7 discusses the LLS work in more detail.

Figure 15 shows a typical video image recorded during the LLS runs. The blade is seen as the lighter colored rectangle on the right side. A smoke stream is visible in the upper half of the picture and was used to visualize the wake. Two counter-rotating vortices are visible in the center of the picture. The vortex images were converted to spatial vortex locations relative to the rotor blade. Figure 16 shows

LLS results for two different rotor thrust conditions, which can be compared to the c_N contours shown in Figure 9a and 9c, respectively. The tunnel wind is from the top of the figure and the blade is outlined at $\psi = 45$ deg. Clockwise (CW), or negative circulation vortices are represented by the unfilled circles. Counter-clockwise (CCW), or positive circulation vortices are represented by the filled circles. Figure 16 shows an increase in the number of CCW vortices captured by the LLS on the advancing side with increasing blade thrust. This increase in vortices results in an increase in the unsteadiness in the c_N values at ψ approximately 45 deg as seen in Fig. 9c.

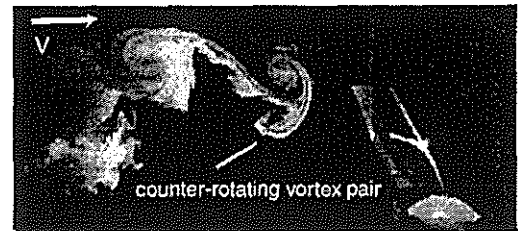


Figure 15. Sample LLS video half-frame.

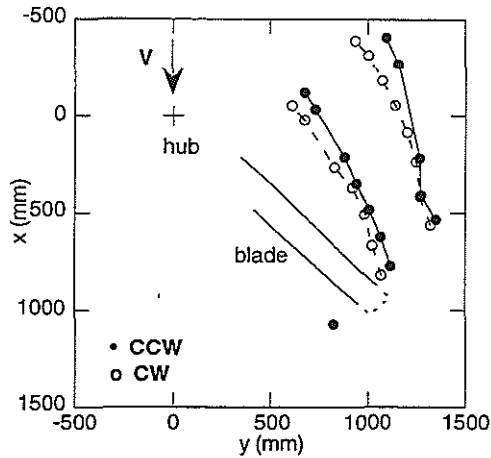
8. Conclusions

The first set of comprehensive blade airloads data for a tiltrotor in forward flight was acquired. Acoustic data, performance data and blade structural loads were acquired simultaneously with the blade airloads. Wake geometry measurements were also made during the test. Variations in shaft angle and rotor thrust were tested for the rotor in simulated descent conditions.

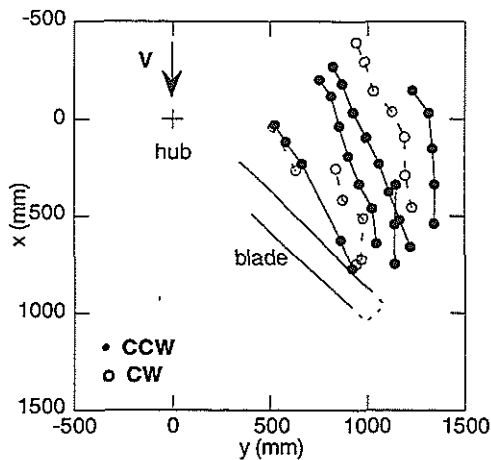
The airloads data acquired have been shown to be highly repeatable between revs for each data point. Comparison of data acquired at the start of each run show repeatability over the length of the test program. Variations with shaft angle and rotor thrust showed negative c_N values for a wide range of operating conditions. This was due primarily to the high blade twist required by the tiltrotor for airplane mode flight and was most noticeable for low thrust conditions.

Correlation between the airloads data and acoustic measurements showed both single and multiple blade-vortex interactions. These interactions were shown as an increase in the unsteadiness in c_N contours, evident for medium and high thrust conditions. Laser light sheet results showed an increase in the number of potential vortex interactions for the higher thrust condition.

The data acquired from this test can be used to validate analytical codes and improve the understanding of tiltrotor airloads, wake structures and acoustic signatures. Designers can utilize this experimental data to model current tiltrotor aerodynamics and to begin to improve the performance and acoustics for future tiltrotor designs.



a) LLS vortex locations for low C_T .



b) LLS vortex locations for high C_T .

Figure 16. LLS vortex locations at low and high thrust.

9. Acknowledgements

The experimental results in this paper were derived from research performed under the auspices of the Tilt Rotor Aeroacoustic Model (TRAM) project and the NASA Short Haul Civil Tiltrotor program SH(CT). The TRAM and SH(CT) programs are led at NASA Ames Research Center by the Army/NASA Rotorcraft Division and Advanced Tiltrotor Technology Project Office, respectively. Other

major funding partners and research participants in the experimental research effort were the U.S. Army Aeroflightdynamics Directorate (AFFD) located at Ames, NASA Langley Research Center Acoustics Division, and Boeing Rotorcraft Division (Mesa, Arizona). In addition, the outstanding support provided by the Duits-Nederlandse Windtunnel staff during the execution of the wind tunnel test was critical to the success of the test.

10. References

1. Marcolini, M. A., Burley, C. L., Conner, D. A., and Acree, C. W., Jr., "Overview of Noise Reduction Technology of the NASA Short Haul (Civil Tiltrotor) Program," SAE paper 962273, International Powered Lift Conference, Jupiter, FL, November 1996.
2. Burley, C.L., Marcolini, M.A., Brooks, T.F., Brand, A.G., Conner, D.A., "Tiltrotor Aeroacoustic Code (TRAC) Predictions and Comparison with Measurements," AHS 52nd Annual Forum, Washington, D.C., June 1996.
3. Johnson, J. L. and Young, L. A., "Tilt Rotor Aeroacoustic Model Project," Confederation of European Aerospace Societies Forum on Aeroacoustics of Rotorcraft and Propellers, Rome, Italy, June 1999.
4. Young, L.A. "Tilt Rotor Aeroacoustic Model (TRAM): A New Rotorcraft Research Facility," AHS International Specialist's Meeting on Advanced Rotorcraft Technology and Disaster Relief, Gifu, Japan, April, 1998.
5. Young, L. A., Booth, Jr., E. R., Yamauchi, G. K., Botha, G. J., and Dawson, S., "Overview of the Testing of a Small-Scale Proprotor," AHS 55th Annual Forum, Montreal, Canada, May 1999.
6. Booth, E. R., Jr., McCluer, M., and Tadghighi, H., "Acoustic Characteristics of a Model Isolated Tiltrotor in the DNW," AHS 55th Annual Forum, Montreal, Canada, May 1999.
7. Yamauchi, G. K., Burley, C. L., Mercker, E., Pengel, K., and JanakiRam, R. D., "Flow Measurements of an Isolated Model Tilt Rotor," AHS 55th Annual Forum, Montreal, Canada, May 1999.
8. Lorber, P., "Blade-Vortex Interaction Data Obtained from a Pressure-Instrumented Model UH-60A Rotor at the DNW," *Journal of the American Helicopter Society*, Vol. 38, No. 3, July 1993.

9. Caradonna, F. X. and Tung, C., "Experimental and Analytical Studies of a Model Helicopter Rotor in Hover," NASA TM 81232, September 1981.
10. Kitaplioglu, C. and Caradonna, F., "Aerodynamics and Acoustics of Blade-Vortex Interaction Using an Independently Generated Vortex," AHS Aeromechanics Specialists Conference, San Francisco, CA, January 1994.
11. Murashige, A., Kobiki, N., Tsuchihashi, A., Nakamura, H., Inagaki, K., and Yamakawa, E., "ATIC Aeroacoustic Model Rotor Test at DNW," 24th European Rotorcraft Forum, Marseilles, France, September 1998.
12. Heffernan, R. M. and Gaubert, M., "Structural and Aerodynamic Loads and Performance Measurements of an SA349/2 Helicopter with an Advanced Geometry Rotor," NASA TM 88370, November 1986.
13. Kufeld, R. M., Balough, D. L., Cross, J. L., Studebaker, K. F., Jennison, C. D., and Bousman, W. G., "Flight Testing the UH-60A Airloads Aircraft," AHS 50th Annual Forum, Washington, D. C., May 1994.
14. Tung, C. and Branum, L., "Model Tilt-Rotor Hover Performance and Surface Pressure Measurement," AHS 46th Annual Forum, Washington, D.C., May 1990.
15. Swanson, A. A. and Light, J. S., "Shadowgraph Flow Visualization of Isolated Tiltrotor and Rotor/Wing Wakes," AHS 48th Annual Forum, Washington, D.C., June 1992.
16. Burley, C. L., Brooks, T. F., Charles, B. D. and McCluer, M., "Tiltrotor Aeroacoustic Predictions and Comparison with TRAM Test Data," 25th European Rotorcraft Forum, Rome, Italy, September 1999.
17. Seidel, M. and Maarsingh, R.A., "Test Capabilities of the German-Dutch Wind Tunnel DNW for Rotors, Helicopters, and V/STOL Aircraft," 5th European Rotorcraft and Powered Lift Aircraft Forum, September 1979.
18. Van Ditshuizen, J. C. A., Courage, G. D., Ross, R. and Schultz K. J., "Acoustic Capabilities of the German-Dutch Wind Tunnel (DNW)," AIAA-83-0146, January 1983.
19. Marcolini, M. A.; Lorber, P. F.; Miller, Jr., W. T. and Covino, Jr., A. F., "Frequency Response Calibration of Recess-Mounted Pressure Transducers," NASA TM 104031, March 1991.
20. Versteeg. M.H.J.B. and Slot, H., "Miniature Rotating Amplifier System for Windtunnel Application Packs 256 Pre-Conditioning Channels in 187 Cubic Inch," 17th International Congress on Instrumentation in Aerospace Simulation Facilities (ICIASF), Naval Postgraduate School, Monterey, CA, September, 1997.